# Corrosion of titanium alloys in primary water of nuclear pressurised water reactor

Q. Bignon, F. Martin, Q. Auzoux, F. Miserque, M. Tabarant, L. Latu-Romain, Y. Wouters

# Corrosion of titanium alloys in primary water of nuclear pressurised water reactor

Quentin BIGNON[1,3], Frantz MARTIN[1], Quentin AUZOUX[1], Frédéric MISERQUE[1], Michel TABARANT[2], Laurence LATU-ROMAIN[3], Yves WOUTERS[3]

[1]Den-Service de la Corrosion et du Comportement des Matériaux dans leur Environnement (SCCME), CEA, Université Paris-Saclay, F-91191, Gif-sur-Yvette, France

[2]Den-Service d'Etudes Analytiques et de Réactivité des Surfaces (SEARS), CEA, Université Paris-Saclay, F-91191, Gif-sur-Yvette, France

[3]Université Grenoble Alpes, CNRS, SIMaP, F-38402 Saint Martin d'Hères, France

## ABSTRACT

Corrosion of three titanium alloys (T40, TA6V and Ti10-2-3) has been studied in primary water conditions for durations going from 24 h to 3499 h. Oxides formed were observed and analysed by X-ray diffraction (XRD), Raman spectroscopy, Scanning Electron Microscopy (SEM), Energy Dispersive X-ray Spectroscopy (EDS), X-ray Photoelectron Spectroscopy (XPS), Glow Discharge - Optical Emission Spectroscopy (GD-OES), Transmission Electron Microscopy (TEM) ASTAR, Photoelectrochemistry (PEC) and nanoindentation. Influence of chemical composition and microstructure of alloys on corrosion mechanisms has been investigated. Oxides of the three alloys were made of a dense layer and surface crystallites. The dense oxide layer of T40 was made of $TiO_2$ rutile whereas it consisted of $TiO_2$ anatase for both TA6V and Ti10-2-3. Surface crystallites of the three alloys were composed of $TiO_2$ anatase and $FeTiO_3$ ilmenite. Oxide dissolution and precipitation phenomenon were found to play a key role in the corrosion mechanisms. Oxygen vacancies were identified as the point defect diffusing in the three alloys dense oxide layer. Oxygen penetration inside the alloy below the oxide layer was not observed.

## INTRODUCTION

Titanium alloys could be good candidates for nuclear Pressurised Water Reactor (PWR) primary circuit structure components because of their low neutron activation and their good mechanical properties. However, corrosion resistance of titanium alloys in primary water conditions is poorly known

High temperature ($T$ > 500 °C) oxidation of titanium alloys in oxygen, in dry air or in water vapour has been extensively studied mainly for aeronautics applications [1]–[11]. Titanium alloys exposure to such environment may involve the formation of different titanium oxides ($TiO_2$, $Ti_3O_5$, $Ti_2O_3$ and TiO). Nevertheless, the most deleterious phenomenon occurring at temperatures above 800 °C is the dissolution of oxygen in the bulk metal ($\alpha$-case) leading to the modification of mechanical properties of titanium alloys [1], [2]. Kofstad *et al.* have determined that more than 80 % of reacted oxygen was dissolved in titanium exposed 30 min at 900 °C to oxygen atmosphere [3]. This process is due to high oxygen solubility in titanium (33 at %) and high diffusion rate of oxygen at elevated temperature.

Few studies have investigated the corrosion behaviour of titanium alloys in liquid water environment at intermediate temperature [12]–[17]. Kaneda *et al.* have studied corrosion resistance of different $\alpha/\beta$ and

β titanium alloys exposed 500 h to supercritical water (25 MPa, 290 – 550 °C). Very thin oxide film (less than 1 µm) covered by dispersed particles were observed at 290 °C for both α/β and β alloys. Oxides compositions were not investigated at this temperature. At 550 °C, film thicknesses observed after 500 h were around 5 µm and 20 µm for β and α/β alloys, respectively. Outer layers of β alloys oxide were enriched in Cr, Mo and Zr alloying elements. The authors attribute the better general corrosion resistance of β alloys as compared to α/β alloys at 550 °C in terms of mass uptake and oxide layer thickness to alloying elements. However, the structure and the nature of oxides layers as well as corrosion mechanisms taking place in water environment at temperatures close to 300 °C are still undetermined.

The present study aims at determining the corrosion mechanisms of three titanium alloys (α, α/β and β-metastable) in PWR primary water environment ($T$ = 300 °C, $P$ = 150 bar, $[H_2]$ = 25 $cm^3$ NTP (Normal Temperature and Pressure).water $kg^{-1}$, theoretical $pH_{300°C}$ = 7.5). The influence of both chemical compositions and microstructures of alloys on corrosion mechanisms was investigated. Specimens were exposed for durations ranging from 24 h to 3499 h in a corrosion loop. The oxide layers grown on the specimen were analysed by X-ray diffraction (XRD), Raman spectroscopy, Energy Dispersive X-ray Spectroscopy (EDS) and Transmission Electron Microscopy (TEM) ASTAR. The growth mechanisms of the oxide layer were studied by Scanning Electron Microscopy (SEM), Glow Discharge - Optical Emission Spectroscopy (GD-OES), X-ray Photoelectron Spectroscopy (XPS) and Photoelectrochemistry (PEC). Finally, the question of the existence of an α-case was then assessed by nanoindentation. Corrosion kinetics measurements and modelling will be published in a separate paper.

# MATERIALS AND PROCEDURES

## *Materials*

Three titanium alloys representative of different metallurgical classes have been studied: T40, TA6V and Ti-10-2-3. T40 is a single phase α alloy also called commercially pure titanium (ASTM grade 2), TA6V or Ti-6Al-4V (ASTM grade 5) is a two-phase α/β titanium alloy and Ti10-2-3 or Ti-10V-2Fe-3Al is a two-phase β metastable alloy. Their chemical compositions are given in Table 1. The three alloys were supplied by TIMET Savoie as billets in mill-annealed state. Final heat treatment temperatures were 675 °C, 730 °C and 760 °C for T40, TA6V and Ti10-2-3 respectively.

The microstructures of the three alloys are given in Figure 1. T40 showed an equiaxed grain microstructure. Average grain size was 60 µm. TA6V and Ti10-2-3 had a finer bimodal microstructure. Electron Backscatter Diffraction (EBSD) analysis were carried out to determine the volumetric α/β phase ratios. TA6V and Ti10-2-3 contained respectively 4 % and 38 % by volume of β phase. Specimens' length, width and thickness were 20 mm, 10 mm and 1 mm, respectively, and machined so that length and thickness of specimens were along radial and longitudinal directions of billets, respectively. EBSD analysis showed that c axis of the α hexagonal unit cell were mainly oriented along the length and the width for T40 and Ti10-2-3 specimens and mainly along the thickness for TA6V specimens. Specimens were SiC paper grounded from grid 1200 to grid 2400, diamond paste (from granulometry 3 µm to 1 µm) and colloidal silica suspensions ($pH$ = 9) polished. Gold deposits of around 1 nm thick were performed with a

Quorum Q 150 R ES metallizer ($I$ = 10 mA, $t$ = 60 s) on dedicated specimens before exposure to primary water to mark initial surface position and determine the growth direction of the oxide scale.

**Table 1: Billets chemical composition (Ti = bal.)**

| wt. % | Al | V | Fe | C | O |
|---|---|---|---|---|---|
| **T40** | 0.01 | 0.01 | 0.03 | 0.003 | 0.16 |
| **TA6V** | 6.38 | 4.12 | 0.16 | 0.008 | 0.17 |
| **Ti10-2-3** | 2.96 | 9.73 | 2.15 | 0.011 | 0.09 |

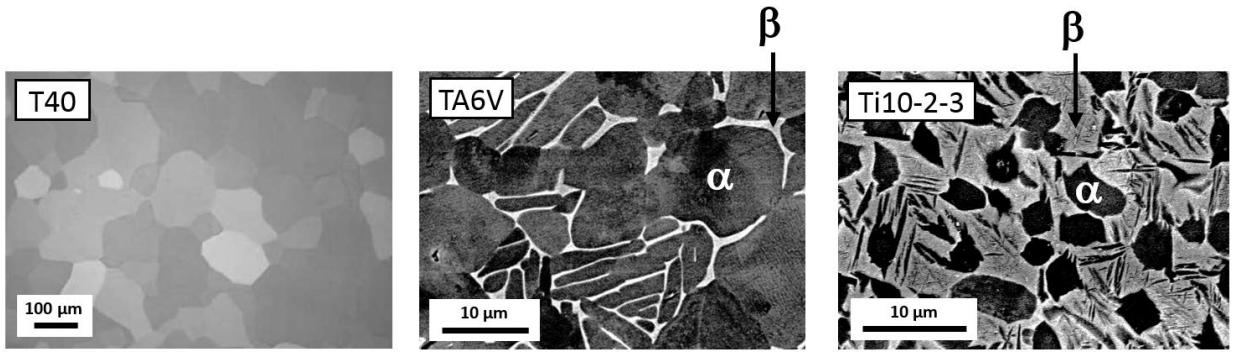


**Figure 1: Microstructure of the studied T40 observed by optical microscopy with polarised light and microstructures of TA6V and Ti10-2-3 observed by SEM in backscattered electrons mode.**

## *Materials exposure to primary water*

Exposure tests were performed in a stainless steel corrosion loop. Specimens were hung inside a vertical cage shape holder made of preoxidised zirconium in order to avoid any galvanic coupling between titanium samples and the stainless steel of the loop. Exposure tests were performed in primary water at 300 °C, 150 bar, 25 $cm^3$ (NTP).water $kg^{-1}$ of dissolved hydrogen and 0.9 wt.ppm of lithium. The heating and cooling rates of the temperature transients were +5 °C.$min^{-1}$ and -1 °C.$min^{-1}$, respectively. The temperature difference between the top and the bottom of the vertical reactor was below 4 °C during thermal transients and below 1 °C at 300 °C. Hydrogen concentration in the water was set by the hydrogen gaseous sky ($P(H_2)$ = 1400 mbar in agreement with Henry's law) inside the cold tank. Lithium was incorporated inside the medium before tests in the form of lithine (LiOH) leading to a theoretical *pH* of 7.5 at 300 °C. The water flow was 5 L.$h^{-1}$ leading to a water speed inside the reactor of 2 mm.$s^{-1}$ during tests. After having been cooled down the whole water volume went through an ion-exchange resin tank in order to capture a part of the corrosion products dissolved in the medium. The ion exchange resin was lithium saturated before the test campaign in order to avoid any variation of lithium concentration during tests. Test durations were 24 h, 89 h, 217 h, 434 h, 834 h, 1632 h and 3499 h. Each exposure duration involved new specimens (no re-exposure for longer times): three samples per alloy for each time, plus one additional gold-deposited specimen of each alloy for the 89 h duration test.

### *Characterisation techniques*

Electrochemical nickel plating were performed on samples before cross sections preparation to prevent oxide scale decohesion. The samples surfaces and cross sections were observed with an Ultra 55 Zeiss Field Emission Gun Scanning Electron Microscopy (SEM) at 5 kV. Oxides diffraction patterns were obtained by analysis of sample surface of 7 x 7 $mm^2$ at grazing incidence (0.8°) with a PANalytical X'Pert PRO MPD X-Ray Diffractometer (XRD). Oxides were also analysed with a Horiba XploRA™PLUS Raman spectroscopy with a laser wavelength of 532 nm, a XFlash Detector 4010 Bruker Energy Dispersive X-ray Spectroscopy (EDS) at 20 kV, a Thermofisher Escalab 250 xi X-ray Photoelectron Spectroscopy (XPS) from Al k$\alpha$ ray (1486.6 eV) and a Profiler 2 Horiba Scientific Glow Discharge – Optical Emission Spectroscopy (GD-OES). XPS was equipped with an $Ar^+$ ion sputtering gun for elementary concentration profiles realisation.

The precession-assisted crystal orientation mapping technique, ASTAR, which is a TEM-based diffraction spot recognition technique [18] was used to acquire oxide phase maps. It was realised on a Transmission Electron Microscope at 200 keV (FEG-TEM, Jeol 2100 F). Transversal cross-sections thin foils were previously prepared with a dual-focused ion beam scanning electron microscope (FIB-SEM, Zeiss Cross Beam NVision 40).

Semiconducting properties of oxide scales were determined by Photoelectrochemistry (PEC). PEC setup was made of an electrochemical glass cell with three electrodes. The working electrode was the oxidised titanium sample to be studied, the reference electrode was a Mercury Sulfate Electrode (MSE) and the counter electrode was made of a platinum sheet. The electrolyte used was $Na_2SO_4$ at the concentration of 0.1 $mol.L^{-1}$. Monochromatic light was provided by a xenon lamp connected to a grating monochromator. The PEC cell was connected to a potentiostat to impose potential conditions. The photocurrent was measured using a lock-in amplifier and a mechanical light chopper. PEC spectra presented in this study were recorded at a light frequency of 15 Hz, at potentials ranging from -420 mV/MSE to +280 mV/MSE and at energies ranging from 2.5 eV to 5 eV.

The potential oxygen enrichment in the alloys under the oxide scale was investigated by nanoindentation (Micro Materials NanoTest$^{TM}$ NTX). Evolution of hardness with depth under the oxide layer was studied thanks to several indent sets realised on samples cross sections. In a set, indents were spaced by 1 µm in sample depth direction and 10 µm laterally. Indent used were Berkovich type indent. The maximum applied force was around 9 mN and indentation depths and widths were around 300 nm and 1 µm, respectively. Polishing procedure of samples cross sections before nanoindentation tests was exactly the same as the one used for all samples before corrosion tests.

## RESULTS

### *Characterisation of the oxide scales*

XRD diffractrograms at grazing incidence of T40, TA6V and Ti10-2-3 after 434 h exposure to primary water are shown in Figure 2. The XRD analysis depth is of the order of few micrometers and the detection limit is around 1 %. Figure 2 indicates that the oxides of the three alloys formed during exposure were composed of $TiO_2$ anatase with tetragonal crystal system and $FeTiO_3$ ilmenite with trigonal crystal system. $TiO_2$ rutile with tetragonal crystal system is detected in T40 oxide only

($2\theta$ = 27.5 °, $d_{110}$ = 3.247 Å). Ti-$\alpha$ phase from the metallic part of the three materials as well as Ti-$\beta$ phase of TA6V and Ti10-2-3 were also identified. The peak located at 43.3 ° was attributed to impurities of metallic copper with cubic crystal system which may come from the stainless steel loop.

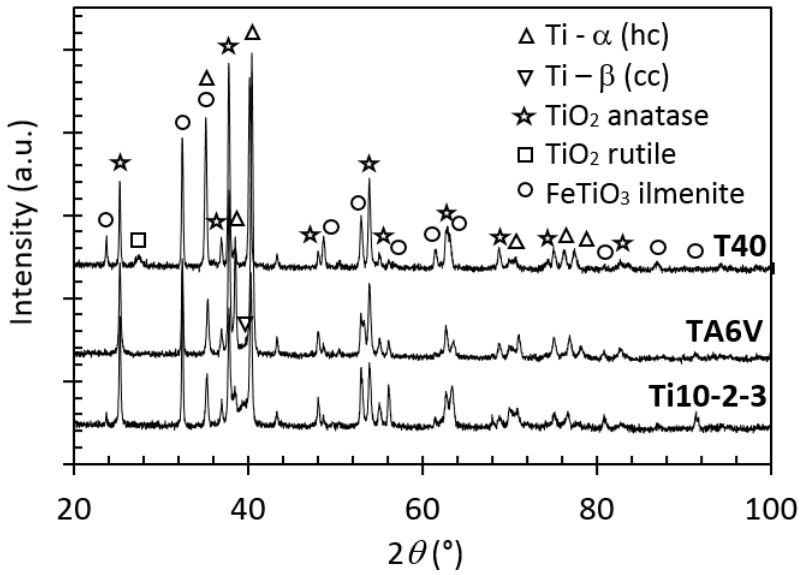


**Figure 2: Diffractograms of T40, TA6V and Ti10-2-3 samples exposed 434 h**

GD-OES profiles carried out on all alloys after 434 h exposure to primary water are shown in Figure 3. In all cases, an oxygen enrichment was evidenced at the surface down to around 0.5 µm depth. For TA6V and Ti10-2-3, no aluminium nor vanadium alloying element were detected in the oxide. This is confirmed by the evolution of Al/Ti and V/Ti ratios with depth (Figure 4). Iron is present in the oxide scale grown on all three alloys. The maximum of Fe/Ti ratio depends on the alloy: it is about 15, 5 and 17 % for T40, TA6V and Ti10-2-3, respectively.

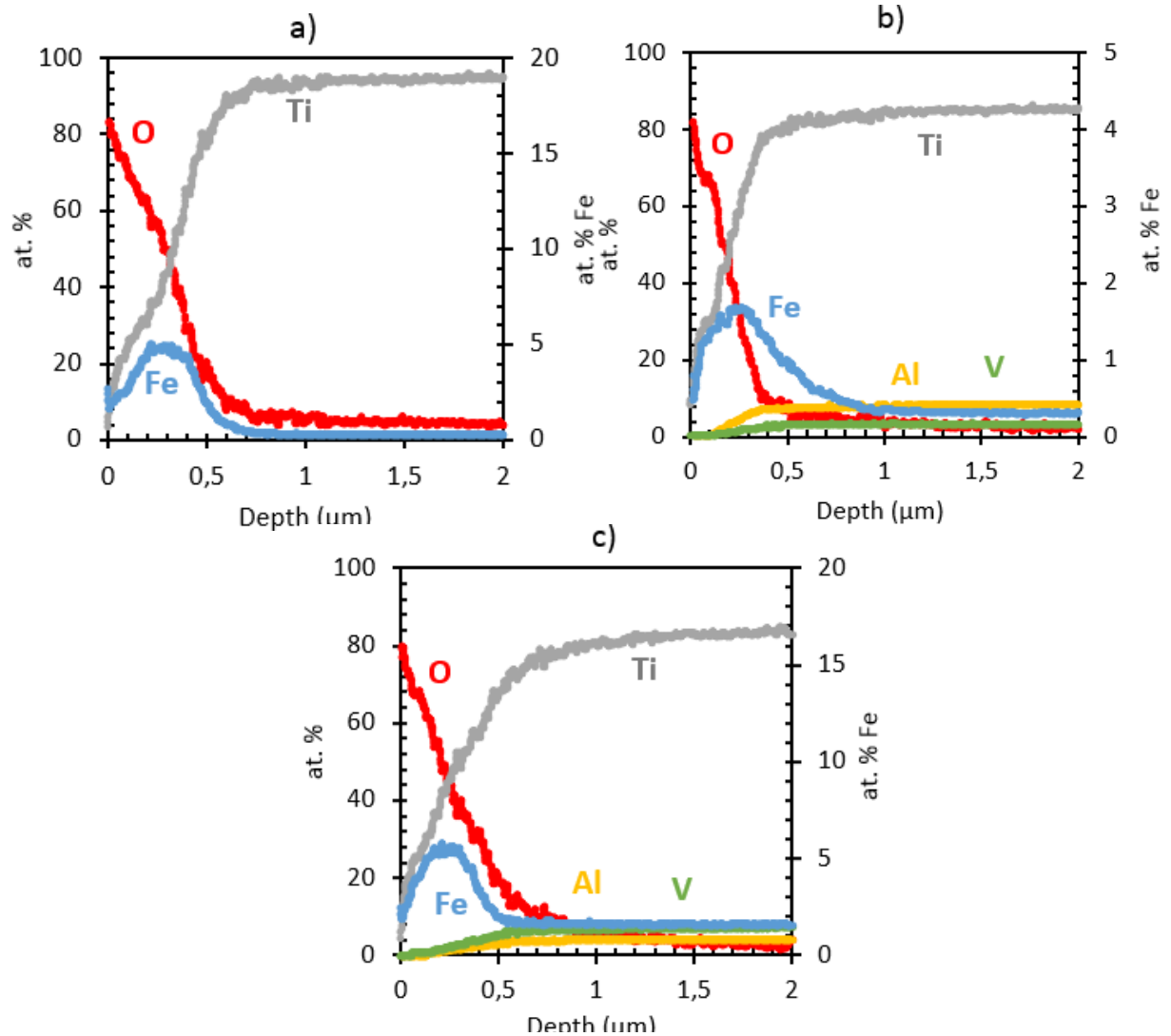


**Figure 3: GD-OES concentrations profiles of samples after 434 h exposure to primary water; a) T40 b) TA6V and c) Ti10-2-3**

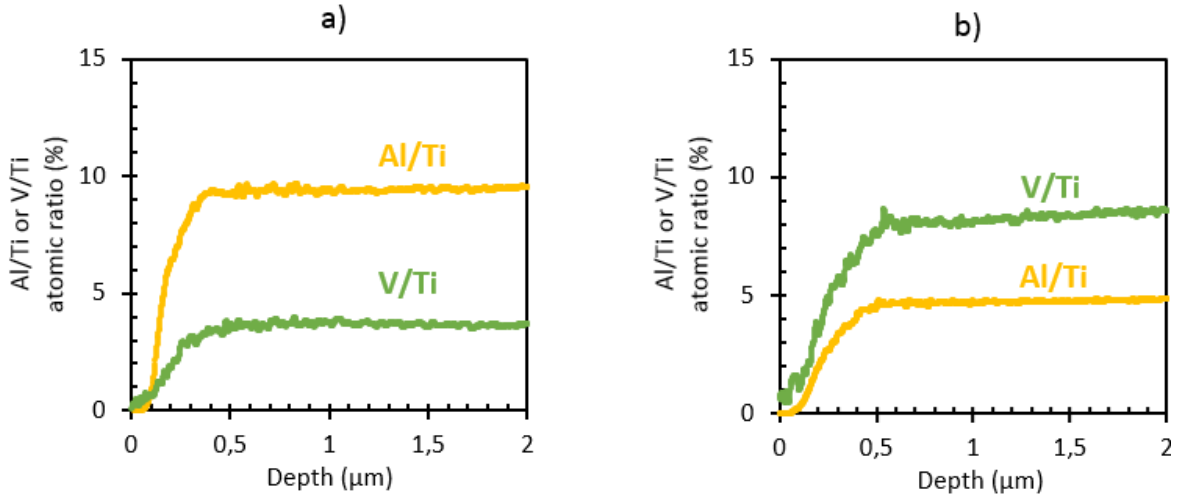


**Figure 4: GD-OES Al/Ti and V/Ti atomic ratio profiles of samples after 434 h exposure; a) TA6V and b) Ti10-2-3**

Figure 5 shows the three alloys sample surfaces and cross sections after 434 h exposure to primary water. For all alloys, observations indicate that the oxide scale is constituted of a dense continuous oxide layer as well as small and large surface oxide crystallites. However, morphologies of the dense continuous oxide layer and small oxide crystallites differ according to the alloy. T40 oxide appears to be constituted of a dense continuous 30 nm-thick oxide layer topped by well-separated small oxide crystallites. TA6V and Ti10-2-3 scales are constituted of a dense continuous oxide layer with joined small oxide crystallites which at this scale were not differentiable from the dense continuous oxide layer. For TA6V and Ti10-2-3, in areas where such small crystallites are absent, the dense oxide layer thickness was estimated around 30 nm. Where small crystallites are present, there is no apparent separation between the dense continuous oxide layer and these small crystallites; the thickness of this overall oxide layer reaching 300 nm locally. Small crystallites' diameter was found of about 1 µm for T40 and lower than 1 µm for both TA6V and Ti10-2-3.

There is also a variation of large crystallites size and distribution depending on the alloy after 434 h. Images analysis indicate that large crystallites diameter averages 3 µm for T40 and Ti10-2-3 and around 10 µm for TA6V. Surface large crystallites densities were estimated around 5000 $mm^{-2}$, 1000 $mm^{-2}$ and 10000 $mm^{-2}$ for T40, TA6V and Ti10-2-3, respectively. Evolution of crystallites size with exposure duration is weak. Nevertheless, the tendency which seems to emerge from surface observations for all alloys is the increase of large crystallites size with exposure duration while small crystallites size stays almost steady.

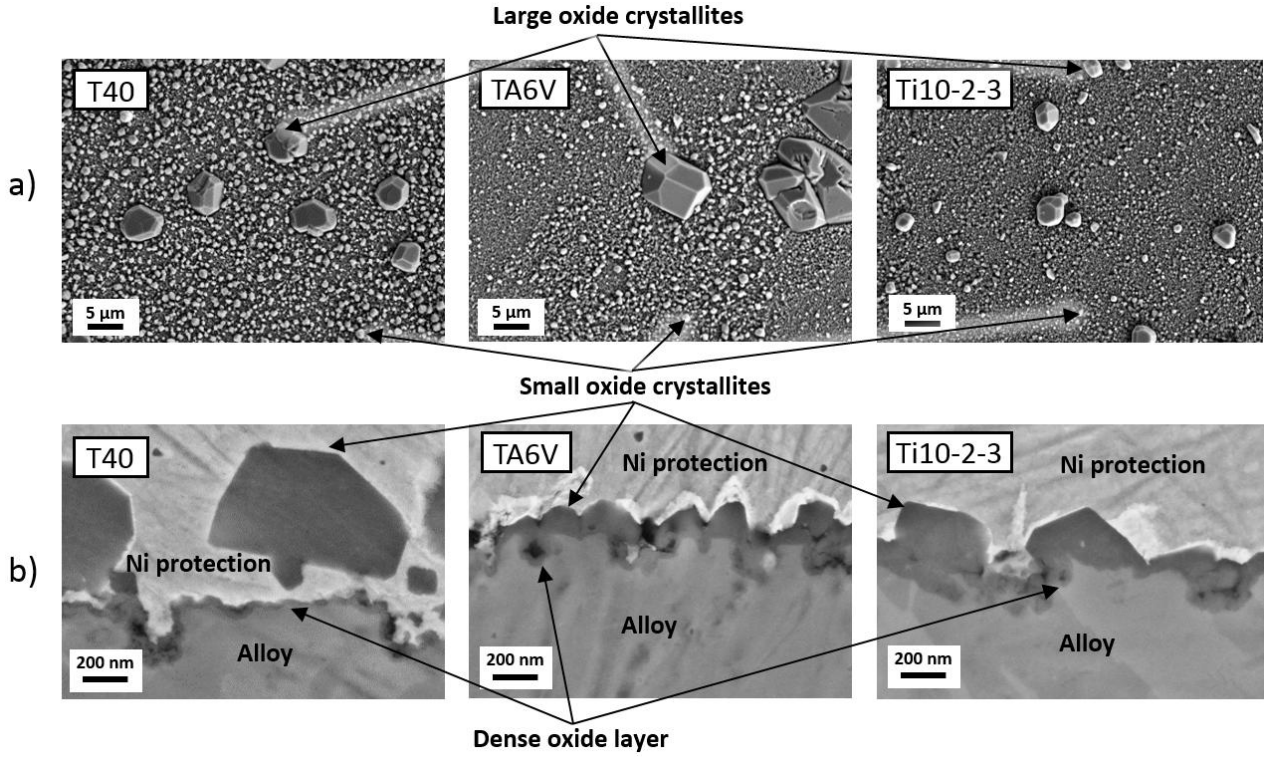


**Figure 5: SEM observation (secondary electrons) of T40, TA6V and Ti10-2-3 samples after 434 h exposure to primary water; a) surface and b) cross sections**

T40 samples cross sections after 217 h, 434 h and 834 h exposure to primary water (Figure 6) reveal that oxide-metal interface tortuosity increases with exposure duration. Corrosion penetration depth reaches 100 nm, 200 nm and 400 nm for 217 h, 434 h and 834 h exposure duration, respectively. The evolutions of TA6V and Ti10-2-3 oxide-metal interface morphologies are similar to the one on T40. For TA6V and Ti10-2-3, penetrations do not seem to be located preferentially in $\alpha$ or $\beta$ phase. Figure 6 also shows that the dense continuous oxide layer thickness of T40 stays around 30 nm during exposure from 217 h to 834 h. The dense continuous oxide layer thickness of TA6V and Ti10-2-3 is also around 30 nm and constant during exposure from 217 h to 834 h.

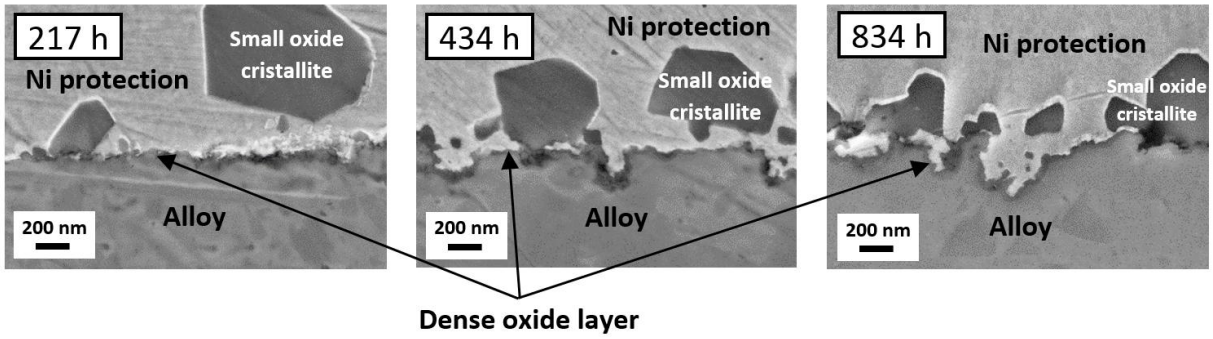


**Figure 6: SEM observation (secondary electrons) of T40 samples cross sections after 217 h, 434 h and 834 h exposure to primary water**

T40 sample cross section after gold markers deposit and 89 h exposure is presented in Figure 7. Gold markers are situated just above the dense oxide layer, demonstrating its inward growth. However, markers are below small crystallites (as shown in Figure 7) and large oxide crystallites. The morphologies of TA6V and Ti10-2-3 cross sections after 89 h exposure with preliminary gold deposit are similar to the one observed on T40.

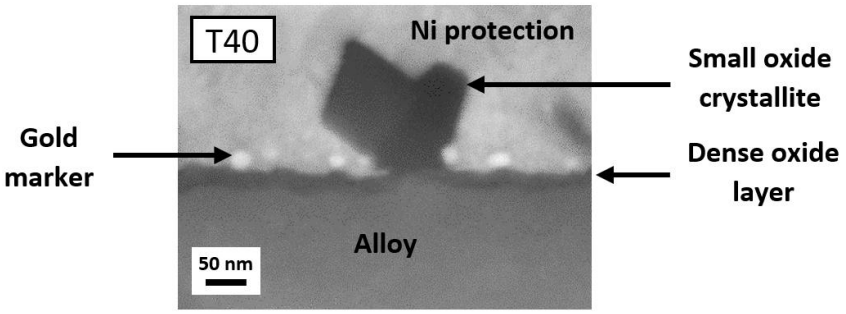


**Figure 7: SEM observation (secondary electrons) of T40 sample cross sections after 89 h exposure to primary water with preliminary gold marker deposit**

EDS mapping of T40 sample surface after 434 h exposure (Figure 8) shows oxygen enrichment of both small and large crystallites. Nevertheless, only large crystallites contain iron. EDS analysis performed on TA6V and Ti10-2-3 samples surfaces lead to the same conclusions. Lateral spatial resolution for the chosen experimental conditions was around 1 µm ($E$ = 20 kV).

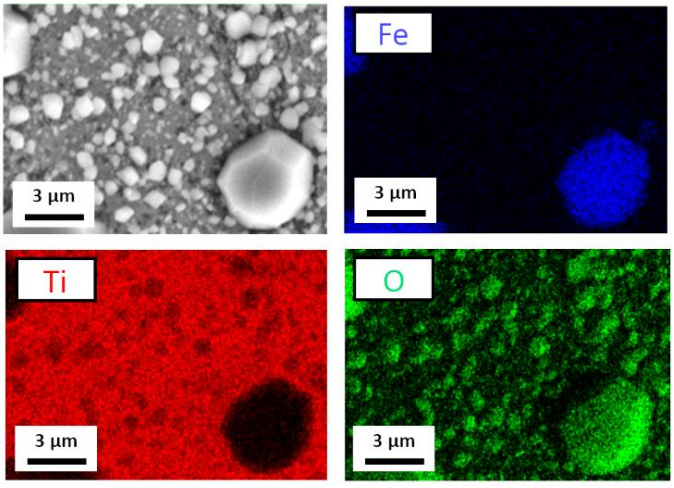


**Figure 8: EDS mapping ($E$ = 20 kV) of T40 sample surface exposed 434 h**

Local Raman analysis of T40 sample surface after 834 h exposure to primary water are presented in Figure 9. Spectra of Figures 9.a) and 9.b) correspond to the signal obtained by focusing the laser beam on small crystallites and large crystallites, respectively. The lateral spatial resolution of Raman analysis is lower than 1 µm and the detection limit is around 1 %. It means that the signal coming from the dense oxide layer is also collected when the laser is focused on small oxide crystallites. Nevertheless, due to the

low volume fraction of the dense oxide layer, the corresponding signal may be undetected. Local Raman analysis indicate that small crystallites/dense oxide layer are mostly made of $TiO_2$ anatase whereas large crystallites are made of $FeTiO_3$ ilmenite. Results were not alloy nor exposure time (834 h or 217 h) dependent.

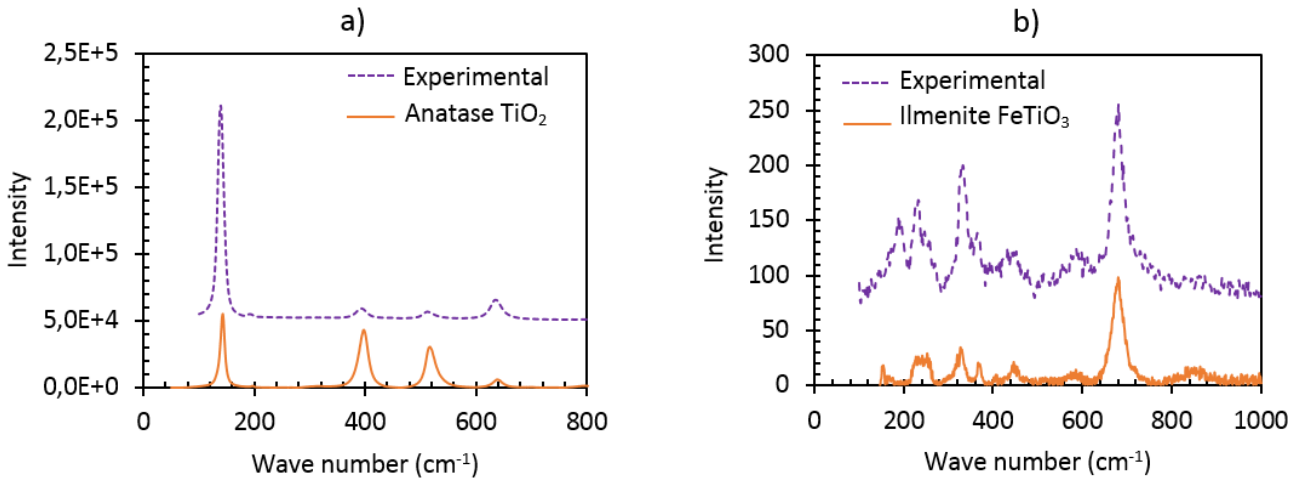


**Figure 9: Raman analysis of T40 sample surface exposed 834 h to primary water (dash lines) ; a) small crystallites and dense oxide layer and b) large crystallites ; solid lines refer to Raman spectra from reference [19] ; a) $TiO_2$ anatase and b) $FeTiO_3$ ilmenite.**

Figure 10 presents ASTAR phase combined to correlation index maps of oxides scale of the three alloys after 434 h. The probe size and the step size measure 1 nm and 3 nm, respectively. The phase map of TA6V was located in a metallic area without β phase. The phase map of the three alloys were performed on areas free from large crystallites. Phase maps show that small crystallites of the three alloys are made of $TiO_2$ anatase. The dense oxide layer grown on T40 is composed of $TiO_2$ rutile (yellow layer) whereas for TA6V and Ti10-2-3 it consists in $TiO_2$ anatase. Grain diameters of both anatase and rutile dense $TiO_2$ scale is in the order of few 10 nm.

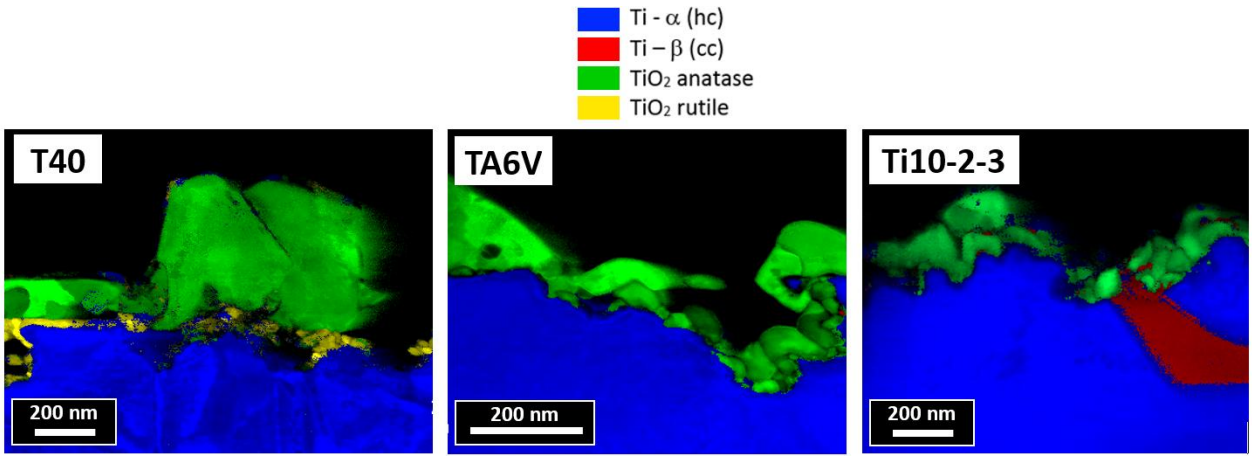


**Figure 10: ASTAR phase combined to correlation index maps of oxide scales on T40, TA6V and Ti10-2-3 samples exposed 434 h to primary water**

Figure 11 illustrates XPS surface spectra of Al-2p core level of both non-exposed and 24 h exposed TA6V samples. XPS characterisation depth is around 10 nm. The analysed surface was around 0.25 $mm^2$. Detection limit is between 0.1 and 1 at. % according to the element. Concerning the non-exposed sample spectra (in red), the peak located at 74.4 eV indicates that the native oxide layer contains aluminium cations (green contribution) [20]. However, the absence of peak at the same binding energy for the 24 h exposed sample spectrum means that no aluminium cation was detected at the oxide scale surface after 24 h exposure. Results obtained for both non exposed and 24 h exposed Ti10-2-3 samples were similar to TA6V ones.

XPS spectra of Al-2p core levels versus etching durations of a TA6V sample exposed 24 h in primary water is plotted in Figure 12. The absence of intensity at the binding energy of 74.4 eV for all etching durations indicate that no aluminium cation is detected in the whole oxide scale after this exposure time. The result obtained for 24 h exposed Ti10-2-3 samples is similar for TA6V.

Vanadium was not detected by XPS analysis in the TA6V native oxide scale nor in the TA6V oxide scale formed after 24 h exposure to media. However, vanadium was detected by XPS in Ti10-2-3 native oxide scale whereas it was not in the Ti10-2-3 oxide scale formed after 24 h exposure to primary water.

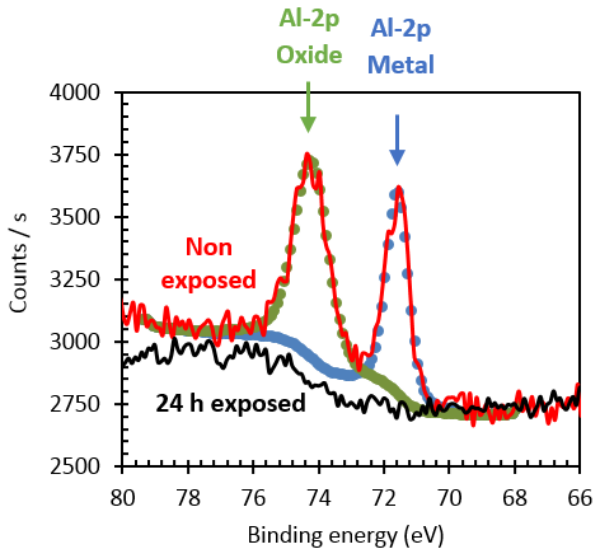


**Figure 11 : Al 2p XPS surface spectra of non-exposed and 24 h exposed TA6V samples**

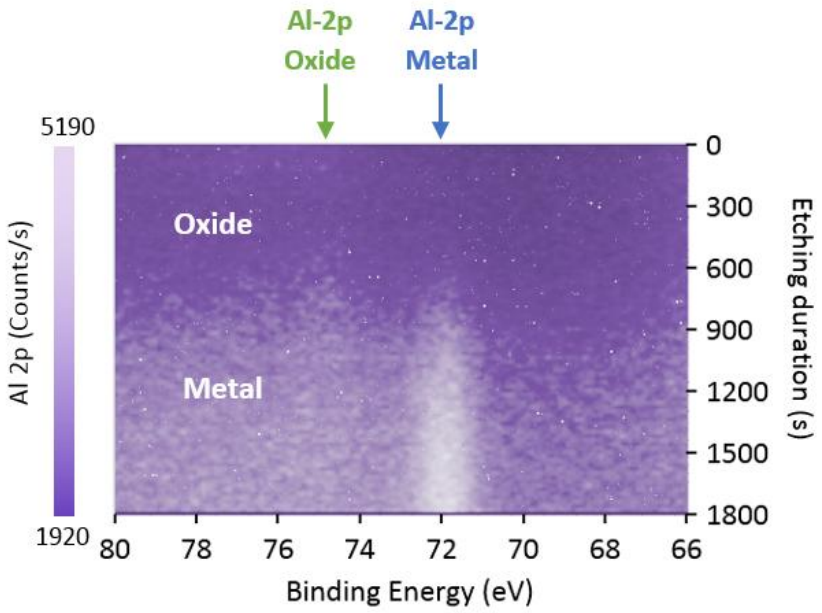


**Figure 12: Al 2p XPS surface spectra of 24 h exposed TA6V samples versus etching duration.**

Evolutions of photocurrent ($I_{ph}$) and dephasing angle ($\phi$) versus incident light energy ($E$) of a T40 sample exposed 3499 h to primary water are shown in Figure 13 a) and b), respectively. Both evolutions are plotted for applied potentials going from -420 mV/MSE towards 280 mV/MSE. $\phi$ is stable with $E$ and shows the presence of a single semiconducting phase in the scale. Figure 13 c) represents the evolution of the photocurrent versus potential for the energy value of 3.76 eV for which the photocurrent is maximum (Figure 13 a)). The photocurrent increases linearly with applied potential. The same kind of evolution is obtained for every sample of the three alloys exposed during 24 h, 434 h and 3499 h.

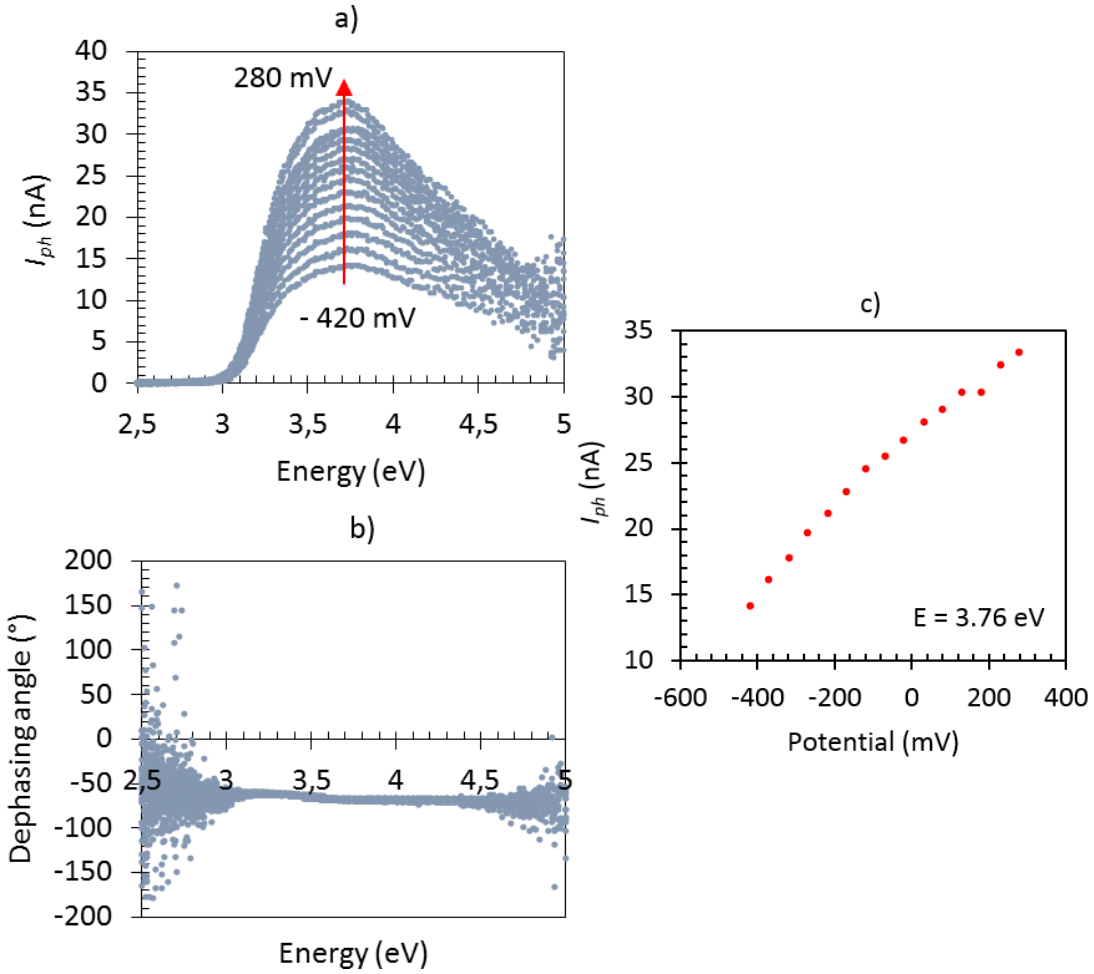


**Figure 13: a) Photocurrent ($I_{ph}$) and dephasing angle ($\phi$) versus incident light energy ($E$) for different potential varying from -420 mV/MSE to 280 mV/MSE of T40 sample after 3499 h exposure. c) Photocurrent versus potential at 3.76 eV.**

Classical linear transform described elsewhere [21], [22] ($(I_{ph}.E)^{0.5}$ vs. $E$) was plotted for all alloys to evaluate oxide bandgap energies ($E_g$). Table 2 presents the bandgap energy values measured for T40, TA6V and Ti10-2-3 oxides layers obtained after 24 h, 434 h and 3499 h exposure. Bandgap energies obtained for TA6V and Ti10-2-3 are centered on 3.2 eV for all investigated exposure durations. The bandgap energy obtained for T40 was smaller than those on TA6V and Ti10-2-3. It decreases from 3.08 eV to 3.00 eV for exposure durations going from 24 h to 3499 h.

**Table 2: Oxides bandgap energies ($E_g$) after 24 h, 434 h and 3499 h exposure to primary water**

| $E_g$ (eV) | T40 | TA6V | Ti10-2-3 |
|---|---|---|---|
| **24 h** | 3.08 | 3.23 | 3.20 |
| **434 h** | 3.02 | 3.24 | 3.25 |
| **3499 h** | 3.00 | 3.18 | 3.19 |

Figure 14 shows the hardness profile of a T40 sample cross section exposed 434 h to primary water obtained by nanoindentation. The profile plotted in the figure is the average of values coming from five different profiles. It indicates that hardness of metal below the oxide layer is constant with depth. The large uncertainty of the first hardness value just below the oxide is due to the fact that some indents encroach upon the oxide and the nickel deposit on top of the oxide. Hardness was not measured on TA6V and Ti10-2-3 samples cross sections because of the overly difference between $\alpha$ and $\beta$ phase hardness.

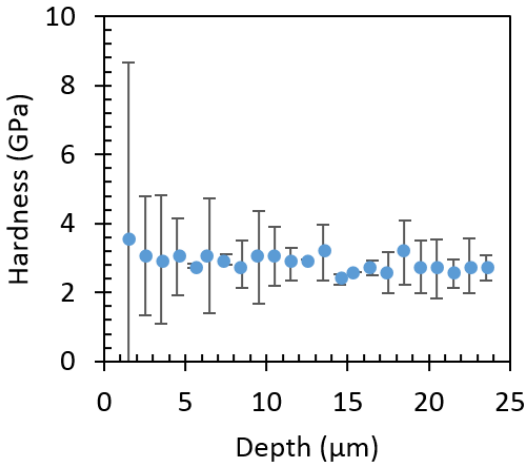


**Figure 14: Nanoindentation hardness profile of T40 sample cross section after 434 h exposure**

## *Similarities and differences between the three alloys oxide scales*

Table 3 shows a summary of the similarities and differences observed after exposure of T40, TA6V and Ti10-2-3 samples to primary water. Several results indicate that some characteristics of the oxide scales formed do not depend on the alloy. Indeed, a dense continuous oxide layer, small oxide crystallites and large crystallites were observed by SEM on the three alloys. Inward growth of the dense continuous oxide layer of all alloys was also evidenced thanks to gold markers. XRD analysis showed that the oxide scale of all alloys contain $TiO_2$ anatase and $FeTiO_3$ ilmenite. Moreover, Raman, EDS and ASTAR analysis enabled to assign these oxide phases to small and large crystallites, respectively. Finally, PEC characterisations showed that oxides of the three alloys are all n-type semiconductors. Concerning the evolution of oxides morphologies and nature with exposure duration, results point out that dense continuous oxide layer thickness and small oxide crystallite diameter remain constant and that large oxide crystallite diameter increases, for all alloys. Oxide-metal interface tortuosity also increases with exposure duration for all alloys. Raman analysis do not reveal any evolution of small and large oxide crystallites nature with exposure duration.

Other results indicate some differences between the oxide characteristics of the studied alloys. XRD analysis revealed the presence of $TiO_2$ rutile in T40 oxide scale only. ASTAR phase map showed that the dense oxide layer of T40 was made of $TiO_2$ rutile and that the dense oxide layer of the two other alloys was made of $TiO_2$ anatase. Moreover, SEM cross section observations point out oxide morphology differences. Indeed, the T40 dense continuous oxide layer is topped by small and large oxide crystallites

whereas small crystallites of TA6V and Ti10-2-3 are part of the dense continuous oxide layer. Finally, a significant difference between the bandgap of the T40 oxide layer and the bandgap of both TA6V and Ti10-2-3 oxide layers was measured by PEC.

**Table 3: Summary of results obtained for the three alloys**

| Techniques | Results | T40 | TA6V | Ti10-2-3 |
|---|---|---|---|---|
| XRD | $TiO_2$ anatase | Yes | Yes | Yes |
| | $TiO_2$ rutile | Yes | No | No |
| | Ilmenite | Yes | Yes | Yes |
| SEM | Inward growth of dense oxide layer | Yes | Yes | Yes |
| | Small crystallites are part of dense oxide layer | No | Yes | Yes |
| Raman | Small crystallites are $TiO_2$ anatase | Yes | Yes | Yes |
| | Large crystallites are $FeTiO_3$ ilmenite | Yes | Yes | Yes |
| ASTAR | Nature of dense oxide layer | $TiO_2$ rutile | $TiO_2$ anatase | $TiO_2$ anatase |
| PEC | n-type semiconduction | Yes | Yes | Yes |
| | $E_g$ | ≈ 3.0 eV | ≈ 3.2 eV | ≈ 3.2 eV |

# DISCUSSION

## *Dissolution and precipitation phenomenon*

The increase of interface tortuosity with time (Figure 6) along with the steadiness of the dense continuous oxide layer thickness indicate that this $TiO_2$ layer undergoes a dissolution phenomenon during exposure to the water at the same time as it grows inwards. It is consistent with the significant value of the $TiO_2$ solubility in water in the conditions of the study (around 1.2 $10^{-8}$ $mol.kg^{-1}$ water [23]). Titanium species potentially formed by dissolution of $TiO_2$ in water at pH 7.5 and 300 °C are $Ti(OH)_4$ and $Ti(OH)_5^-$ hydroxides [24].

The presence of $TiO_2$ anatase crystallites at the dense oxide layer surface of all alloys for all exposure durations indicates that dissolved titanium hydroxides have then precipitated. These species locally reached their solubility limit in spite of the use of ion-exchange resin. It could result from the low water flow (5 $L.h^{-1}$) and the resulting low water speed inside reactor (2 $mm.s^{-1}$). Water flow was maybe not high enough to prevent enrichment in hydroxides inside reactor, especially in the vicinity of the sample surfaces. Solubility of a species may vary with allotropic form and size of the crystal where it comes from.

Indeed, small crystals are generally more soluble than big ones because of the increase of the specific surface energy with decreasing crystal size [25]. It could explain why $TiO_2$ dense layer may dissolve and why hydroxides may precipitate into $TiO_2$ crystallites at the same time.

$FeTiO_3$ ilmenite crystallites certainly originate from the co-precipitation of titanium and iron hydroxides dissolved in medium. It is unlikely that iron hydroxides come from samples oxide dissolution. Indeed, ilmenite crystallites were found in an undifferentiated way on all alloy samples even though iron is not an alloying element of T40. Moreover, the main source of iron is stainless steel loop oxide dissolution.

## *Presence of aluminium in the $TiO_2$ oxide layer of TA6V and Ti10-2-3?*

GD-OES concentration profiles for TA6V and Ti10-2-3 (Figure 3 and Figure 4) do not detect aluminium in the global oxide scale. Yet, it is not possible to conclude whether the dense continuous oxide layer close to the metal is enriched in alloying elements or not by GD-OES analysis alone. Indeed, the roughness of the oxide scales leads to a blurry concentration profile of all elements. Aluminium cations were detected by XPS analysis in the native oxide scale (before exposition) (Figure 11) whereas they were not in the TA6V oxide scale after exposure to medium (Figure 12).

The 25 cc TPN $H_2.kg^{-1}$ water set experimentally led to a ratio of water molecule on hydrogen molecule activities ($a(H_2O)/a(H_2)$) around 1000. This value which is indicative of the redox characteristic of the water is much higher than the ratio of the frontier stability domain of Al and $Al_2O_3$ at 300°C ($a(H_2O)/a(H_2) = 1.10^{-27}$) [26], [27]. It means that aluminium oxide is widely thermodynamically stable in the experimental conditions. Therefore it is believed that aluminium cations are formed and are present in the inwards growing $TiO_2$ oxide scale although they are not detected by XPS analysis. Indeed, the volume fraction of dense continuous oxide layer is low in comparison to the overall oxide volume and the aluminium minimum detectable fraction by XPS analysis is relatively high (due to the low sensibility factor of aluminium). The absence of aluminium enrichment in the metal just below the oxide scale (Figure 4) support this hypothesis.

Studies of high temperature oxidation of titanium alloys in gaseous environment indicate various distribution of alumina inside titanium oxide scales. On one hand, alumina grains were found to be finely scattered through $TiO_2$ scale [1], [7], [10]. On the other hand, an alumina layer was observed at the external $TiO_2$ interface. Kaneda *et al.* who studied corrosion of titanium alloys in supercritical water at 550 °C also observed an alumina layer at the external $TiO_2$ interface [12]. Thus, alumina was never observed at the interface between $TiO_2$ and the metal. Even though temperature involved in these studies are higher than 300 °C, it could be suggested that, in the present study, aluminium cations diffusion from the metal/$TiO_2$ interface towards the $TiO_2$/water interface occurred during exposure of TA6V and Ti10-2-3 samples at 300 °C to primary water.

Finally, the high solubility of aluminium oxides in water at 300 °C and pH 7.5 (around $10^{-3}$ $mol.kg^{-1}$ water [28]) may explain the dissolution of aluminium cations as soon as they reach the oxide/water interface. Thus, the external side of the oxide scale would never be enriched in aluminium cations, which is consistent with the fact they were not detected by XPS analysis.

For TA6V, vanadium was not detected in the native oxide scale nor in the oxide scale formed after 24 h exposure to media. However, vanadium was detected by XPS in Ti10-2-3 native oxide scale whereas it was not in the Ti10-2-3 oxide scale formed after 24 h exposure to primary water. As aluminium oxide

$Al_2O_3$, vanadium oxides like $V_2O_5$ or $VO_2$ are thermodynamically stable in the experimental conditions. As for aluminium, there was no vanadium enrichment in the metal just below the oxide scale (Figure 4). Motte *et al.* as well as Kaneda *et al.* who studied corrosion of TA6V in air between 850 °C and 950 °C and in supercritical water at 500 °C, respectively, founded vanadium dispersed in the whole $TiO_2$ oxide scale. Thus, it could be suggested that vanadium cations, as aluminium cations, were formed and were present in the dense $TiO_2$ oxide scale of TA6V and Ti10-2-3 and were dissolved inside media as soon their reach oxide/water interface.

## *Causes and consequences of the rutile or anatase formation*

XRD analysis revealed the presence of rutile on T40 oxide only. ASTAR phase maps show that the dense oxide layer grown on T40 was made of rutile. These results are consistent with bandgap measured by PEC for T40 oxide ($E_g$ ≈ 3.0 eV). Indeed, this value is close to bandgap value of rutile found in literature ($E_g$(rutile) ≈ 2.95 eV) [29]. In the same way, the presence of the dense $TiO_2$ anatase layer on TA6V and Ti10-2-3 oxides revealed on ASTAR phase maps is consistent with the bandgap value ($E_g$ ≈ 3.2 eV) which is in good agreement with values found for anatase in literature ($E_g$ (anatase) ≈ 3.2 eV) [29].

The fact that the dense $TiO_2$ rutile layer of T40 was not detected by Raman analysis means its concentration is lower than the detection limit of Raman (≈ 1 %) in the volume analysed. The volumic ratio of T40 dense continuous oxide layer on the overall oxide is very low according to its thickness (≈ 30 nm).

Rutile is for all temperature and pressure conditions the thermodynamic stable phase of $TiO_2$. However, low temperature prevents the anatase to rutile transformation (ART) due to kinetics. ART temperature varies from 400 °C to 1000 °C depending both on oxidation environment and impurities in the oxide [30]. Hydrogen atmosphere as well as alkaline and transition metal ions impurities in the oxide scale as $Li_2O$ was found to increase the ART kinetics [10], [30], [31]. It was suggested it could be due to the increase of oxygen vacancies number by hydrogen atmosphere and alkaline and transition metal doping. Vanadium doping was also found to increase ART kinetics [32]. On the contrary, oxidation in $O_2$ was found to inhibit the transformations by filling oxide vacancies [10]. In the same way, Vásquez *et al.* have pointed out that aluminium doping do stabilise $TiO_2$ anatase phase with respect to rutile phase [33].

The water used in the present study contained lithium and hydrogen. It is then suggested that lithium and/or hydrogen were incorporated (in very low concentration) in the dense oxide layer of all alloys samples leading to a decrease of the ART temperature. The ART temperature may have reached values lower than 300 °C explaining the rutile presence in dense oxide layer of T40. It is also suggested that concentration of some alloying element cations as aluminium which diffused inside TA6V and Ti10-2-3 dense oxide layer may have been high enough to increase ART temperature and then stabilise anatase regarding rutile. The absence of aluminium in T40 chemical composition may then explain the rutile dense oxide layer of T40.

The difference in the allotropic form of the dense continuous layer formed on T40 on one hand and on TA6V and Ti10-2-3 on the other hand could be the cause of the difference in oxide morphologies between T40 and the two other alloys. Indeed, TA6V and Ti10-2-3 small oxides crystallites may be part of the dense oxide layer because of their identical allotropic form (anatase), favouring epitaxial growth. On the contrary, T40 small oxide crystallites may be on the top of the dense oxide layer because of their different allotropic form (anatase and rutile, respectively). Thus, hydroxide precipitation phenomenon

may have involved small crystallites nucleation and growth for T40 and small crystallites growth only for TA6V and Ti10-2-3.

### *Oxygen penetration in the metal?*

GD-OES oxygen concentration profiles do not exhibit any oxygen enrichment in the metal bulk below the oxide scale for the three alloys after 434 h exposure (Figure 3). Nanoindentation results obtained on T40 for the same exposure time (Figure 14) are also consistent with the absence of significant oxygen penetration in the metal beyond 1 µm. Indeed, oxygen diffusion in the metal would have enhanced the hardness proportionally to its concentration [19].

This result is consistent with the low diffusion coefficient of oxygen in $\alpha$ titanium at 300 °C. It varies from $2.6\ 10^{-19}$ cm².s$^{-1}$ to $8.8\ 10^{-18}$ cm².s$^{-1}$ according to literature [34], [35]. Theoretical diffusion depth calculated accordingly $(2(D.t)^{1/2})$ varies from 10 to 70 nm for a 434 h duration exposure. Such oxygen penetrations are undetectable by nanoindentation and GD-OES analysis because of the resolution limit of these experimental techniques. Several studies described titanium oxide dissolution linked to the oxygen diffusion in the metal bulk at temperature higher than 380 °C - 400 °C [36]–[38]. It means that degradation of titanium linked to an oxygen enriched area formation does not seem to be an issue at 400 °C.

To the authors' knowledge, no data is available on the diffusion coefficient of oxygen in $\beta$ titanium phase at 300 °C. Nevertheless, diffusion of oxygen in $\beta$ phase at higher temperature (800 °C) is around 100 times faster than in $\alpha$ phase [5], [39], [40]. However, no $\alpha$-case formation was observed by SEM on TA6V and Ti10-2-3 samples cross sections for all exposure durations. Thus, it could be suggested that oxygen diffusion in $\beta$ phase at 300 °C is also low enough to prevent any oxygen enriched area formation.

### *Point defect diffusing in dense oxide layer*

T40 sample exposure to primary water with prior gold marker deposit indicates the inward growth of the $TiO_2$ dense oxide layer (Figure 7). However, gold markers appear to be located below small oxide crystallites. It is suggested that the inner part of the oxide grew by oxidation process and that the outer part of the oxide (oxide crystallites) was formed by the precipitation of titanium hydroxides. The oxidation mechanisms of TA6V and Ti10-2-3 also involved an inward growth of the oxide layer. Finally, oxide layer grown by oxidation process of the three alloys involved an anionic growth.

The anionic growth of the dense oxide layer could be attributed to both interstitial oxygen and oxygen vacancies point defects diffusion. PEC characterisations performed on samples indicate the increase of the photocurrent ($I_{ph}$) with applied potential (Figure 13 c)). Such an evolution is the evidence of the n-type semiconductivity of the characterised oxide. This result is consistent with $TiO_2$ conduction types determined in several studies [41] [42]. Thus, it is possible to conclude that the main point defects responsible for the growth of $TiO_2$ oxide layer are oxygen vacancies. Nevertheless, more characterisations would be necessary to determine the species diffusing inside oxygen vacancies from the external interface toward the internal interface of the oxide layer. In literature, these species are suggested to be oxygen anions or hydroxide anions in dry and water vapour [2] environment, respectively.

# CONCLUSION

Polished samples of T40, TA6V and Ti10-2-3 titanium alloys have been exposed to primary water ($T$ = 300 °C, $P$ = 150 bar, [$H_2$] = 25 cc TPN.kg$^{-1}$ of water, [$Li$] = 0.9 wt. ppm, theoretical $pH$ = 7.5) for durations ranging from 24 h to 3499 h.

- Oxide scale developed on all three alloys is made of a continuous 30 nm thick layer topped by small and large cirstallites. T40 oxide scale is made of a dense continuous $TiO_2$ rutile layer topped by small $TiO_2$ anatase and large $FeTiO_3$ ilmenite crystallites. The TA6V and Ti10-2-3 small $TiO_2$ anatase crystallites are part of the continuous $TiO_2$ anatase layer. TA6V and Ti10-2-3 dense oxide layer are also topped by large ilmenite crystallites. After 434 h exposure, ilmenite crystallites diameter reach 10 µm, anatase crystallites diameter is around 1 µm for T40 and lower than 1 µm for TA6V and Ti10-2-3.
- Presence of crystallites and the increase of the interface tortuosity with exposure time as well as the constant dense oxide layer thickness with exposure time demonstrates the extent of oxide dissolution and hydroxide precipitation phenomenon.
- Corrosion penetration depth reaches around 400 nm for the three alloys after 834 h exposure. For TA6V and Ti10-2-3, penetrations do not seem to be located preferentially in $\alpha$ or $\beta$ phase.
- Oxygen diffusion inside the metal below the oxide layer was limited owing to the low temperature involved.
- Inward growth and n-type semiconductivity of all alloys oxides have been observed and measured. Thus, oxygen vacancies were the main point defect diffusing inside the dense continuous $TiO_2$ layer.

It is suggested that aluminium cations were formed and diffused from the metal/$TiO_2$ interface toward the $TiO_2$/media interface during exposure of TA6V and Ti10-2-3 samples. Aluminium cations may have dissolved as soon as they reached the oxide/media interface because of their high solubility in water in such conditions. It is suggested that rutile may have been formed on T40 because of the effect of hydrogen or lithium oxide doping coming from the water. It is also suggested that only $TiO_2$ anatase was formed on TA6V and Ti10-2-3 because of aluminium doping coming from alloys. Further investigations will be focused on dissolution and corrosion kinetics.

# ACKNOWLEDGEMENTS

The authors wish to thank Etienne Amblard, Claire Berthier, Sylvie Poissonnet and Frédéric Datcharry from CEA Saclay for their precious contributions on experimental and characterisations ressources.

# REFERENCES


[1] I. Gurrappa, 'An oxidation model for predicting the life of titanium alloy components in gas turbine engines', *J. Alloys Compd.*, vol. 389, no. 1–2, pp. 190–197, 2005.

[2] Y. Wouters, A. Galerie, and J.-P. Petit, 'Thermal oxidation of titanium by water vapour', *Solid State Ion.*, vol. 104, no. 1, pp. 89–96, 1997.

[3] P. Kofstad, P. B. Anderson, and O. J. Krudtaa, 'Oxidation of titanium in the temperature range 800–1200°C', *J. Common Met.*, vol. 3, no. 2, pp. 89 – 97, 1961.

[4] P. Kofstad, K. Hauffe, and H. Kjollesdal, 'Investigation on the oxidation mechanism of titanium', *Acta Chem. Scand.*, vol. 12, no. 2, pp. 239–266, 1958.

[5] C. J. Rosa, 'Oxygen diffusion in alpha and beta titanium in the temperature range of 932° to 1142°C', *Metall. Trans.*, vol. 1, no. 9, pp. 2517–2522, 1970.

[6] H. L. Du, P. K. Datta, D. B. Lewis, and J. S. Burnell-Gray, 'Air oxidation behaviour of Ti6Al4V alloy between 650 and 850°', *Corros. Sci.*, vol. 36, no. 4, pp. 631–642, 1994.

[7] F. Motte, C. Coddet, P. Sarrazin, M. Azzopardi, and J. Besson, 'A comparative study of the oxidation with water vapor of pure titanium and of Ti-6Al-4V', *Oxid. Met.*, vol. 10, no. 2, pp. 113–126, 1976.

[8] A. M. Chaze and C. Coddet, 'Influence of aluminium on the oxidation of titanium between 550 and 750 °C', *J. Common Met.*, vol. 157, no. 1, pp. 55 – 70, 1990.

[9] A. M. Chaze and C. Coddet, 'Influence of chromium on the oxidation of titanium between 550° and 700°C', *Oxid. Met.*, vol. 21, no. 3, pp. 205–231, 1984.

[10] P. Sarrazin, F. Motte, J. Besson, and C. Coddet, 'Mechanism of oxidation of titanium and alloy ti-6al-4v by water-vapor', *J. -Common Met.*, vol. 59, no. 2, pp. 111–117, 1978.

[11] H. Guleryuz and H. Cimenoglu, 'Oxidation of Ti–6Al–4V alloy', *J. Alloys Compd.*, vol. 472, no. 1, pp. 241 – 246, 2009.

[12] J. Kaneda *et al.*, 'General corrosion properties of titanium based alloys for the fuel claddings in the supercritical water-cooled reactor', in *Proceedings of the 12th International Conference on Environmental Degradation of Materials in Nuclear Power System—Water Reactors, The Minerals, Metals & Materials Society, Salt Lake City, UT*, 2005, pp. 1409–1418.

[13] J.-S. Lu, Z.-Y. Mao, J.-Y. Zhang, C.-A. Ma, X.-B. Mao, and X.-H. Li, 'Corrosion of titanium in supercritical water oxidation environments', *Trans. Nonferrous Met. Soc. China*, vol. 12, pp. 1054–1057, 2002.

[14] X. Tang *et al.*, 'Corrosion behavior of nickel base alloys, stainless steel and titanium alloy in supercritical water containing chloride, phosphate and oxygen', *Chem. Eng. Res. Des.*, vol. 100, pp. 530–541, 2015.

[15] S. Y. Park, 'Hydrogen pick-up and corrosion behavior of Ti-alloy (PT-7M) in ammonia water chemistry', Korea, 2004, pp. 915–916.

[16] B. S. Choi, 'Design Features of SMART Water Chemistry', Pittsburgh USA, 2004, pp. 39–45.

[17] I. V. Gorynin, 'Titanium alloys for marine application', *Mater. Sci. Eng. A*, vol. 263, no. 2, pp. 112–116, 1999.

[18] E. F. Rauch and M. Véron, 'Automated crystal orientation and phase mapping in TEM', *Mater. Charact.*, vol. 98, pp. 1 – 9, 2014.

[19] T. Armbruster and R. M. Danisi, Eds., *Highlights in mineralogical crystallography*. Berlin ; Boston: Walter de Gruyter GmbH, 2016.

[20] L. P. H. Jeurgens, W. G. Sloof, F. D. Tichelaar, C. G. Borsboom, and E. J. Mittemeijer, 'Determination of thickness and composition of aluminium-oxide overlayers on aluminium substrates', *Appl. Surf. Sci.*, vol. 144–145, pp. 11 – 15, 1999.

[21] W. W. Gärtner, 'Depletion-Layer Photoeffects in Semiconductors', *Phys Rev*, vol. 116, no. 1, pp. 84–87, 1959.

[22] M. A. Butler, 'Photoelectrolysis and physical properties of the semiconducting electrode WO2', *J. Appl. Phys.*, vol. 48, no. 5, pp. 1914–1920, 1977.
[23] K. G. Knauss, M. J. Dibley, W. L. Bourcier, and H. F. Shaw, 'Ti (IV) hydrolysis constants derived from rutile solubility measurements made from 100 to 300 C', *Appl. Geochem.*, vol. 16, no. 9, pp. 1115–1128, 2001.
[24] W. G. Cook and R. P. Olive, 'Pourbaix diagrams for chromium, aluminum and titanium extended to high-subcritical and low-supercritical conditions', *Corros. Sci.*, vol. 58, pp. 291–298, 2012.
[25] M. Kahlweit, 'Ostwald ripening of precipitates', *Adv. Colloid Interface Sci.*, vol. 5, no. 1, pp. 1 – 35, 1975.
[26] *HSC thermodata software version 4.0*. .
[27] O. Kubaschewski and C. B. Alcock, *Metallurgical Thermochemistry*. Pergamon Press, 1979.
[28] P. Bénézeth, D. A. Palmer, and D. J. Wesolowski, 'Aqueous high-temperature solubility studies. II. The solubility of boehmite at 0.03 m ionic strength as a function of temperature and pH as determined by in situ measurements', *Geochim. Cosmochim. Acta*, vol. 65, no. 13, pp. 2097–2111, 2001.
[29] Y. Wouters, 'Oxydation thermique des metaux dans la vapeur d'eau. Cas du nickel et du titane', Thèse de doctorat, Institut National Polytechnique de Grenoble, 1996.
[30] F. C. Gennari and D. M. Pasquevich, 'Kinetics of the anatase–rutile transformation in TiO2 in the presence of Fe2O3', *J. Mater. Sci.*, vol. 33, no. 6, pp. 1571–1578, 1998.
[31] R. D. Shannon, 'Phase Transformation Studies in TiO2 Supporting Different Defect Mechanisms in Vacuum-Reduced and Hydrogen-Reduced Rutile', *J. Appl. Phys.*, vol. 35, no. 11, pp. 3414–3416, 1964.
[32] N. Khatun *et al.*, 'Anatase to rutile phase transition promoted by vanadium substitution in TiO 2 : A structural, vibrational and optoelectronic study', *Ceram. Int.*, vol. 43, no. 16, pp. 14128–14134, Nov. 2017.
[33] G. C. Vásquez *et al.*, 'Influence of Fe and Al doping on the stabilization of the anatase phase in $TiO_2$ nanoparticles', *J Mater Chem C*, vol. 2, no. 48, pp. 10377–10385, 2014.
[34] D. David, E. Garcia, and G. Beranger, 'Measurement of diffusion-coefficient of oxygen in alpha titanium between 460-degrees and 750-degrees-c by use of the nuclear-reaction o-16(d,p)o-17x', *Comptes Rendus Acad. Sci. Ser. Ii*, vol. 294, no. 16, pp. 945–948, 1982.
[35] J. W. Rogers, K. L. Erickson, D. N. Belton, R. W. Springer, T. N. Taylor, and J. G. Beery, 'Low temperature diffusion of oxygen in titanium and titanium oxide films', *Appl. Surf. Sci.*, vol. 35, no. 1, pp. 137 – 152, 1988.
[36] Y. Mizuno *et al.*, 'Temperature dependence of oxide decomposition on titanium surfaces in ultrahigh vacuum', *J. Vac. Sci. Technol. Vac. Surf. Films*, vol. 20, no. 5, p. 1716, 2002.
[37] T. Smith, 'Oxidation of titanium between 25 degrees c and 400 degrees c', *Surf. Sci.*, vol. 38, no. 2, pp. 292–312, 1973.
[38] G. Lu, S. L. Bernasek, and J. Schwartz, 'Oxidation of a polycrystalline titanium surface by oxygen and water', *Surf. Sci.*, vol. 458, no. 1, pp. 80–90, 2000.
[39] M. Song, S. Han, D. Min, G. Choi, and J. Park, 'Diffusion of oxygen in β-titanium', *Scr. Mater.*, vol. 59, no. 6, pp. 623–626, 2008.
[40] R. P. Elliott, 'Diffusion in Titanium and Titanium Alloys', DTIC Document, 1962.
[41] Y. Wouters, A. Galerie, and J.-P. Petit, 'Photoelectrochemical Study of Oxides Thermally Grown on Titanium in Oxygen or Water Vapor Atmospheres', *J. Electrochem. Soc.*, vol. 154, no. 10, p. C587, 2007.
[42] Y.-K. Choi, 'Thin Titanium Dioxide Film Electrodes Prepared by Thermal Oxidation', *J. Electrochem. Soc.*, vol. 139, no. 7, p. 1803, 1992.